Chemical Engineering Science 259 (2022) 117795

Contents lists available at ScienceDirect

Chemical Engineering Science

journal homepage: www.elsevier.com/locate/ces

Transport in turbulent, recurrent flows: Time-extrapolation and statistical symmetrization

T. Lichtenegger *, S. Abbasi, S. Pirker

Department of Particulate Flow Modelling, Johannes Kepler University, Altenberger Str. 69, 4040 Linz, Austria

HIGHLIGHTS

- Time-extrapolation of field time series using recurrence plots.
- Fast and accurate simulations of bubble transport in submerged, turbulent jets.
- Simulation of conditions in between recorded databases by statistical interpolation.
- Data augmentation to enforce long-term system symmetries from short time series.

ARTICLE INFO

Article history:
Received 23 February 2022
Received in revised form 2 May 2022
Accepted 8 June 2022
Available online 14 June 2022

Keywords:
Submerged double-jet
Bubble transport
Multi-scale problems
Data-assisted simulations
Time-extrapolation
Recurrence CFD

ABSTRACT

We investigate bubble dynamics in a submerged double-jet as an example of weakly coupled, Lagrangian transport. The setup resembles continuous casting of steel at Reynolds numbers Re = 136 000 to Re = 272 000. Using short time series of flow fields obtained from large-eddy simulations (LES) with a discrete bubble model, we calculate a database of transport patterns and time-extrapolate them to long durations in the framework of recurrence CFD (rCFD). A dedicated averaging procedure along bubble trajectories allows us to study their transport with large steps at little numerical costs and monitor their spatial distribution. Besides time-extrapolation for fixed Re with a single database, we demonstrate how several time series can be combined to (i) enforce symmetries and (ii) approximately model conditions in between. We compare bubble volume fraction fields and total hold-up obtained from LES and from rCFD and find very good to satisfying agreement with speed up factors of more than 500.

1. Introduction

Turbulent flows constitute a prime example for complex, spatio-temporal multi-scale dynamics. Comparatively stable large-scale vortices decay into mid- and finally small-sized eddies with decreasing life times such that short-lived, small-scale fluctuations characterize the local behavior of such flows. The non-trivial interplay between structures of different scales gives rise to an overall highly complex evolution, which still poses serious modeling and simulation challenges. While the governing equations of motion (EOMs), the Navier–Stokes equations, are well-known, their solution requires extremely fine meshes and small time steps, which limits direct numerical simulations (DNS) to small-scale, short-term studies. The extreme multi-scale nature of high-Re flows can be mitigated by spatial filtering, which amounts in LES (Pope, 2000) that account for the influence of sub-grid scales with empirical correction terms and can be solved with coarser resolution and larger time steps. Nevertheless, large-scale investigations or long-term observations are hardly possible. The increase of computer power, especially the availability of a huge number of processors to carry out massively parallel simulations, has been pushing the limits of LES to systems of appreciable size. However, long-term studies have remained elusive, which is particularly regrettable if one is interested in slow processes like species or heat transport or certain types of chemical conversion on top of a highly dynamic background. For such applications, approximations to speed up calculations need to be imposed so that long durations can be covered. Such methods include reduced-order models based on proper orthogonal decomposition (POD) (e.g. Georgaka et al., 2020; Hijazi et al., 2020; Stabile et al., 2019; Star et al., 2021; Zimmermann and Görtz, 2012) and/or machine-learning techniques like Gaussian processes regression (Xiao et al., 2019; Yang and Xiao, 2020) or various types of neural networks (e.g. Lui and Wolf, 2019; Murata et al., 2020; Pawar et al., 2019; Rahman

* Corresponding author.
E-mail addresses: thomas.lichtenegger@jku.at (T. Lichtenegger), sanaz.abbasi@jku.at (S. Abbasi), stefan.pirker@jku.at (S. Pirker).

https://doi.org/10.1016/j.ces.2022.117795
0009-2509/

Nomenclature

Greek letters

α	[ ]	volume fraction
β	[kg/s]	drag correlation
δ	[ ]	Kronecker delta
Δ	[m]	filter width
ϵ	[ ]	recurrence threshold
ν	$[\mathrm{m}^2/\mathrm{s}]$	viscosity
ρ	$[\mathrm{kg}/\mathrm{m}^3]$	density
$\boldsymbol{\sigma}$	$[\mathrm{kg}/(\mathrm{ms}^2)]$	stress tensor
τ	[s]	duration, time range
$\boldsymbol{\tau}$	$[\mathrm{kg}/(\mathrm{ms}^2)]$	deviatoric stress tensor
$\boldsymbol{\Omega}$	[1/s]	rate-of-rotation tensor

Latin symbols

C	[ ]	model constant
$\dot{\boldsymbol{d}}$	[m/s]	displacement field
d	[m]	diameter
D	$[\mathrm{m}^2/\mathrm{s}]$	diffusivity
D	[ ]	distance norm/matrix
Δt	[s]	time step
$\boldsymbol{f}$	$[\mathrm{kg}/(\mathrm{m}^2\mathrm{s}^2)]$	force density
$\boldsymbol{F}$	$[\mathrm{kgm}/\mathrm{s}^2]$	force
$\boldsymbol{g}$	$[\mathrm{m}/\mathrm{s}^2]$	gravity
$\boldsymbol{I}$	[ ]	identity matrix
$\boldsymbol{J}$	[ ]	jump matrix
k	$[\mathrm{m}^2/\mathrm{s}^2]$	kinetic energy
m	[kg]	bubble mass
N	[ ]	integer number
$\mathcal{N}$	[ ]	distance norm's normalization constant
P	[ ]	probability
p	$[\mathrm{kg}/(\mathrm{ms}^2)]$	pressure
R	[ ]	recurrence norm/matrix
$\boldsymbol{r}$	[m]	position
$\boldsymbol{S}$	[1/s]	rate-of-strain tensor
$\boldsymbol{S}$	[ ]	shift matrix
$\boldsymbol{t}$	[ ]	system state vector
$\boldsymbol{T}$	[ ]	transfer matrix
$\boldsymbol{u}$	[m/s]	filtered velocity field
$\boldsymbol{U}$	[m/s]	unfiltered velocity field
$\boldsymbol{v}$	[m/s]	bubble velocity

Subscripts/Superscripts

b	bubble
C	coarse mesh
ext	external
f	fluid
fluc	fluctuation
nn	nearest neighbor
res	residual
rec	recurrence
rnd	random
sgs	sub-grid scale
t	terminal

List of abbreviations

CFD	computational fluid dynamics
DNS	direct numerical simulation
LES	large eddy simulation
DNS	direct numerical simulation
POD	proper orthogonal decomposition
Re	Reynolds number
rCFD	recurrence CFD
Sc	Schmidt number

et al., 2019; San and Maulik, 2018). A general overview of turbulence modeling with data-assisted techniques has been provided by Duraisamy et al., 2019.

In contrast to these highly sophisticated and elaborate approaches, we have developed the conceptually very simple method rCFD specifically targeted at recurrent systems, where characteristic patterns keep reappearing albeit in a completely irregular fashion. Based on a short time series of flow fields obtained with any detailed simulation technique, rCFD extrapolates this series with an iterated method of analogues (Cecconi et al., 2012). Instead of solving the EOMs to obtain the future evolution of the latest flow state, one determines the most similar previous configuration within the series and uses the corresponding evolution. If this procedure is applied to e.g. the velocity of a turbulent flow, one can easily calculate long-term transport processes on top of the field series by solving only the passive transport equation without the need to deal with momentum and pressure. Besides its simplicity, rCFD has two major advantages: It is long-term stable per construction (the extrapolated sequence contains only physically valid flow fields), and it involves no black-box calculations which might be hard to interpret and make it difficult to trace errors.

In previous work on turbulent flows, rCFD was employed to investigated passive species transport in vortex shedding behind obstacles (Abbasi et al., 2020; Du et al., 2020) and in submerged jets (Abbasi et al., 2020; Pirker et al., 2020) at high Re. Especially the latter type of system provides a very interesting playground for rCFD. Under confinement, submerged jets can exhibit low-frequency oscillations (Mosavati et al., 2020; Lawson and Davidson, 2001; Wen et al., 2014; Righolt et al., 2015), which poses a serious challenge for a description only based on short time series. With this work, we significantly deepen our understanding and improve the foundations of rCFD by applying it to the example of coupled bubble transport by a turbulent double-jet at $\mathrm{Re} = 136\,000$ to $\mathrm{Re} = 272\,000$. More specifically, we address and present solutions to the following issues: (i) Even though rCFD does not require to solve the momentum and pressure equations, transport of a passive or weakly coupled species is subject to rapid velocity fluctuations and therefore limited by very small time steps. (ii) Slow modes, e.g. low-frequency jet oscillations, can easily exceed to scope of a database consisting of a short time series. (iii) Turbulent flows often lead to extremely noisy and hence almost structureless distance matrices, which seems to contradict the basic idea of rCFD to identify similar flow states and employ knowledge about their past behavior. (iv) It would be highly desirable to simulate conditions not directly covered by a previously recorded database, e.g. for time-varying boundary conditions.

We stress that even though the configuration of our test case is reminiscent of continuous casting of steel (cf. Section 3), the above findings apply to any type of turbulent flow, where the long-term behavior is of interest. Equipped with these insights, it is possible to carry out very fast simulations of transport processes under turbulent conditions.

Our work is organized as follows. In Section 2, we review the fluid-mechanical EOMs in the presence of discrete bubbles and summarize the theoretical background of rCFD. The case setup for our simulations is described in Section 3 with the obtained results provided and discussed in Section 4. Finally, we draw conclusions and point out current limitations of the methodology in Section 5.

2. Theoretical background

We briefly review the EOMs of a fluid with a dispersed, secondary phase like bubbles or solid particles. Simulations that fully resolve the flow fields around (and some of them also within, for the case of bubbles) each discrete element (Blais et al., 2016; Baltussen et al., 2017) are very costly and limited to small system sizes. Therefore, we take the unresolved point of view that permits the description of larger-scale problems. For the sake of simplicity, we restrict ourselves to the incompressible case with constant density ρ_f, but note that this does not impact any of our subsequent findings. In the second subsection, we provide the reader with an overview of the rCFD methodology consisting of distance matrix, recurrence path and time-extrapolated long-term simulation. We put a special focus on new developments relevant to the problem of bubble transport in a turbulent jet, in particular on large-step transport on rapidly varying fields and on the issue of utterly noisy distance plots without clear recurrences.

2.1. EOMs of a turbulent fluid with a dispersed bubble phase

2.1.1. Fluid EOMs

In the presence of a dispersed, secondary phase, the unresolved flow model is obtained by locally filtering the Navier–Stokes equations for a fluid with velocity $\boldsymbol{U}_\mathrm{f}$ with a normalized filter function $g(r)$ that falls off after a few bubble or particle diameters. This leads to the structurally similar set of equations (Anderson and Jackson, 1967)

$$\frac{\partial}{\partial t}\alpha_\mathrm{f} + \nabla\cdot\alpha_\mathrm{f}\boldsymbol{u}_\mathrm{f} = 0 \tag{1}$$

$$\frac{\partial}{\partial t}\alpha_\mathrm{f}\boldsymbol{u}_\mathrm{f} + \nabla\cdot\alpha_\mathrm{f}\boldsymbol{u}_\mathrm{f}\boldsymbol{u}_\mathrm{f} = \frac{1}{\rho_\mathrm{f}}\left(\nabla\cdot\boldsymbol{\sigma}_\mathrm{f}^{(0)} - \nabla\cdot\boldsymbol{\tau}_\mathrm{res} + \boldsymbol{f}_\mathrm{b-f} + \boldsymbol{f}_\mathrm{ext}\right) \tag{2}$$

for the filtered velocity $\boldsymbol{u}_\mathrm{f} \equiv g * \boldsymbol{U}_\mathrm{f}$. Compared to the incompressible, single-phase Navier–Stokes equations, Eqs. (1) and (2) differ in several regards. The volume fraction field α_f accounts for the locally available volume not occupied by the secondary phase, and $\boldsymbol{f}_\mathrm{b-f}$ describes the momentum exchange between the phases. $\boldsymbol{f}_\mathrm{ext}$ contains all forces of external origin such as gravity $\boldsymbol{f}_\mathrm{grav} = \rho_\mathrm{f}\alpha_\mathrm{f}\boldsymbol{g}$. For the sake of simplicity, we consider a Newtonian fluid with

$$\boldsymbol{\sigma}_\mathrm{f}^{(0)} \equiv -p_\mathrm{f}\boldsymbol{I} + \rho_\mathrm{f}\nu_\mathrm{f}\left(\nabla\boldsymbol{u}_\mathrm{f} + (\nabla\boldsymbol{u}_\mathrm{f})^\dagger\right) - \frac{2}{3}\rho_\mathrm{f}\nu_\mathrm{f}\boldsymbol{I}\nabla\cdot\boldsymbol{u}_\mathrm{f} \tag{3}$$

$$\equiv -p_\mathrm{f}\boldsymbol{I} + \rho_\mathrm{f}\boldsymbol{\tau}, \tag{4}$$

where p_f is the fluid pressure, $\boldsymbol{I}$ the unit matrix, ν_f the kinematic viscosity and $\boldsymbol{\tau}$ the deviatoric stress.

In the filtering procedure, the nonlinear convective term gives rise to the residual stress tensor

$$\boldsymbol{\tau}_\mathrm{res} = g*(\boldsymbol{U}_\mathrm{f}\boldsymbol{U}_\mathrm{f}) - (g*\boldsymbol{U}_\mathrm{f})(g*\boldsymbol{U}_\mathrm{f}) = g*(\boldsymbol{U}_\mathrm{f}\boldsymbol{U}_\mathrm{f}) - \boldsymbol{u}_\mathrm{f}\boldsymbol{u}_\mathrm{f}, \tag{5}$$

which needs to be closed in analogy to single-phase turbulence (Pope, 2000). The Boussinesq approach connects the residual stresses to the rate-of-strain tensor

$$\boldsymbol{S} \equiv \frac{1}{2}\left(\nabla\boldsymbol{u}_\mathrm{f} + (\nabla\boldsymbol{u}_\mathrm{f})^\dagger\right) \tag{6}$$

with a sub-grid scale viscosity ν_sgs, which leads to

$$\boldsymbol{\sigma}_\mathrm{f} \equiv \boldsymbol{\sigma}_\mathrm{f}^{(0)} - \boldsymbol{\tau}_\mathrm{res} = -p_\mathrm{f}\boldsymbol{I} + 2\rho_\mathrm{f}(\nu_\mathrm{f} + \nu_\mathrm{sgs})\boldsymbol{S} - \frac{2}{3}\rho_\mathrm{f}(\nu_\mathrm{f} + \nu_\mathrm{sgs})\boldsymbol{I}\mathrm{tr}(\boldsymbol{S}). \tag{7}$$

A multitude of closure models for ν_sgs can be found in literature. Some of them were tailored to specific applications, while others may be regarded as more general. In this work, we employ the wall-adapting local eddy viscosity (WALE) (Nicoud and Ducros, 1999) which exhibits the correct y^3 near-wall scaling per construction. In addition to the rate-of-strain tensor $\boldsymbol{S}$, it takes the rate-of-rotation tensor

$$\boldsymbol{\Omega} \equiv \frac{1}{2}\left(\nabla\boldsymbol{u}_\mathrm{f} - (\nabla\boldsymbol{u}_\mathrm{f})^\dagger\right) \tag{8}$$

to determine the sub-grid-scale viscosity in terms of

$$\xi^{(d)} \equiv \boldsymbol{S}\cdot\boldsymbol{S} + \boldsymbol{\Omega}\cdot\boldsymbol{\Omega} - \frac{1}{3}\boldsymbol{I}(\boldsymbol{S}:\boldsymbol{S} - \boldsymbol{\Omega}:\boldsymbol{\Omega}) \tag{9}$$

$$\nu_\mathrm{sgs} = (C_\mathrm{w}\Delta)^2\frac{\left(\xi^{(d)}:\xi^{(d)}\right)^{3/2}}{(\boldsymbol{S}:\boldsymbol{S})^{5/2} + \left(\xi^{(d)}:\xi^{(d)}\right)^{5/4}} \tag{10}$$

$$C_\mathrm{w} = 0.325. \tag{11}$$

Δ, a characteristic length scale of the flow, is obtained from the local cell volume via $\Delta = (V_c)^{1/3}$. The unresolved kinetic energy may be estimated with (Shukla and Dewan, 2019)

$$k_\mathrm{sgs} \equiv \left(\frac{\nu_\mathrm{sgs}}{C_\mathrm{k}\Delta}\right)^2 \tag{12}$$

$$C_\mathrm{k} = 0.094. \tag{13}$$

2.1.2. Bubble EOMs

Bubbles are deformable and therefore more complicated than rigid particles (Ford and Loth, 1998). However, if they are not too large, they can legitimately be modeled as spherical, discrete elements with constant density ρ_b (Sujatha et al., 2017). A bubble with mass m_i and velocity $\boldsymbol{v}_i$ obeys

$$\frac{d}{dt}\boldsymbol{r}_i = \boldsymbol{v}_i \tag{14}$$

$$\frac{d}{dt}m_i\boldsymbol{v}_i = \sum_j \boldsymbol{F}_{i,j}^{(\mathrm{b-b})} + \boldsymbol{F}_i^{(\mathrm{b-f})} + \boldsymbol{F}_i^{(\mathrm{ext})}, \tag{15}$$

where $\boldsymbol{F}_{i,j}^{(\mathrm{b-b})}$ is the interaction between two bubbles i and j in contact, $\boldsymbol{F}_i^{(\mathrm{b-f})}$ models the forcing of the surrounding fluid and $\boldsymbol{F}_i^{(\mathrm{ext})}$ contains external contributions such as gravity $\boldsymbol{F}_i^{(\mathrm{grav})} = V_i\rho_\mathrm{b}\boldsymbol{g}$ or wall forces $\boldsymbol{F}_i^{(\mathrm{wall})}$. A detailed analysis of the various contributions to the bubble-fluid interaction such as pressure gradient, drag, lift and virtual mass forces can be found in the work of Jain et al., 2013.

A high-fidelity description requires all these force contributions, and any adaptions need to be considered carefully. In the present investigation, we chose to impose significant simplifications because the main focus of our work concerned the time-extrapolation of previously calculated time series *independent* from the model with which these data had been obtained. Hence, we retained only pressure gradient and drag,

$$\boldsymbol{F}_i^{(\mathrm{b-f})} \approx -V_i\nabla p_\mathrm{f} + (\boldsymbol{u}_\mathrm{f} - \boldsymbol{v}_i)\beta(\boldsymbol{u}_\mathrm{f} - \boldsymbol{v}_i) \tag{16}$$

$$\approx -V_i\rho_\mathrm{f}\boldsymbol{g} + (\boldsymbol{u}_\mathrm{f} - \boldsymbol{v}_i)\beta(\boldsymbol{u}_\mathrm{f} - \boldsymbol{v}_i) \tag{17}$$

in our derivation, where we further assumed that the hydrostatic outweighs the dynamic pressure. If bubbles are much lighter than the surrounding fluid, they can follow the acting forces so fast that they quickly reach their local equilibrium velocity $\boldsymbol{v}_i^{(0)}$, and $\frac{d}{dt}m_i\boldsymbol{v}_i$

vanishes. Hence, the right-hand side of Eq. (15) needs to vanish, too. Neglecting bubble-wall and bubble–bubble interaction (which is permissible for low concentrations), the interphase force needs to balance the bubble's weight,

$$\boldsymbol{F}_i^{(\mathrm{b-f})} + \boldsymbol{F}_i^{(\mathrm{grav})} = 0, \tag{18}$$

so that

$$V_i(\rho_\mathrm{b} - \rho_\mathrm{f})\boldsymbol{g} \approx -\left(\boldsymbol{u}_\mathrm{f} - \boldsymbol{v}_i^{(0)}\right)\beta\left(\boldsymbol{u}_\mathrm{f} - \boldsymbol{v}_i^{(0)}\right). \tag{19}$$

This equation is satisfied if the local bubble and fluid velocities differ by the so-called terminal rising velocity $\boldsymbol{v}_\mathrm{t}$ which is oriented in opposite direction of gravity and constant for a given bubble size. $\boldsymbol{v}_\mathrm{t}$ can either be determined from the solution of Eq. (19) for a choice of drag correlation β, or it can be measured experimentally.

Once the terminal rising velocity is known, it is not necessary anymore to deal with an ODE of the type Eq. (15). Instead, we may directly solve

$$\frac{d}{dt}\boldsymbol{r}_i = \boldsymbol{u}_\mathrm{f}(\boldsymbol{r}_i) + \boldsymbol{v}_\mathrm{t} + \boldsymbol{v}_\mathrm{fluc}, \tag{20}$$

which is numerically much simpler, especially for the very stiff problem of low bubble and high fluid density. The last term in Eq. (20) accounts for turbulent dispersion due to sub-grid fluctuations, which is determined by the Schmidt number Sc_sgs. The discrete counterpart of a passive species diffusing with $D_\mathrm{sgs} = \nu_\mathrm{sgs}/\mathrm{Sc}_\mathrm{sgs}$ is given by a random walk with

$$\boldsymbol{v}_\mathrm{fluc} = \boldsymbol{n}_\mathrm{rnd}\sqrt{\frac{6D_\mathrm{sgs}}{\Delta t}}, \tag{21}$$

where Δt is the step size in the solution procedure of Eq. (20) and $\boldsymbol{n}_\mathrm{rnd}$ a randomly oriented unit vector. Due to the random nature of $\boldsymbol{n}_\mathrm{rnd}$, bubbles in high-concentration regions are automatically dispersed, which prevents overpacking and allows to neglect any repulsive bubble–bubble interaction $\boldsymbol{F}_{i,j}^{(\mathrm{b-b})}$ for not too high volume fractions. However, bubbles (almost) in contact with a wall require special treatment. Any component of $\boldsymbol{v}_\mathrm{t} + \boldsymbol{v}_\mathrm{fluc}$ in normal direction towards the wall needs to be discarded.

Finally, the bubble-fluid interaction $\boldsymbol{F}_i^{(\mathrm{b-f})}$ lets us evaluate the interphase force density $\boldsymbol{f}_\mathrm{b-f}$ in Eq. (2), which has not been determined yet. Momentum conservation requires

$$\boldsymbol{f}_\mathrm{b-f}(\boldsymbol{r}) = -\sum_i g(|\boldsymbol{r} - \boldsymbol{r}_i|)\boldsymbol{F}_i^{(\mathrm{b-f})}. \tag{22}$$

In the present case, we use Eq. (19) to get

$$\boldsymbol{f}_\mathrm{b-f}(\boldsymbol{r}) = \sum_i g(|\boldsymbol{r} - \boldsymbol{r}_i|)V_i\rho_\mathrm{b}\boldsymbol{g} = (1-\alpha_\mathrm{f})\rho_\mathrm{b}\boldsymbol{g}. \tag{23}$$

Then, the fluid momentum equation takes the simplified form

$$\frac{\partial}{\partial t}\alpha_\mathrm{f}\boldsymbol{u}_\mathrm{f} + \nabla\cdot\alpha_\mathrm{f}\boldsymbol{u}_\mathrm{f}\boldsymbol{u}_\mathrm{f} = \frac{1}{\rho_\mathrm{f}}(\nabla\cdot\boldsymbol{\sigma}_\mathrm{f} + (1-\alpha_\mathrm{f})(\rho_\mathrm{b} - \rho_\mathrm{f})\boldsymbol{g}), \tag{24}$$

where a constant term $\rho_\mathrm{f}\boldsymbol{g}$ has been moved into the definition of pressure. For very low ratios of $\rho_\mathrm{b}/\rho_\mathrm{f}$, the interphase interaction Eq. (23) is small and the main influence of the bubble on the fluid phase stems from volume displacement and a correspondingly decreased mixture density.

In our simplified modeling strategy, Eq. (24) needs to be solved together with Eq. (1) and Eq. (20).

2.2. Recurrence CFD

2.2.1. Distance norm

A flow's similarity at two times t_i, t_j can be assessed by defining a distance function $D(t_i, t_j)$. There is no unique, best choice for $D(t_i, t_j)$, but a previous investigation demonstrated the importance of field data instead of single probing points (Lichtenegger, 2018). Hence, reasonable choices for a turbulent flow compare the velocity or the sub-grid-scale kinetic energy,

$$D_u(t_i, t_j) = \frac{1}{\mathcal{N}}\int d^3r\left(\boldsymbol{u}(\boldsymbol{r}, t_i) - \boldsymbol{u}(\boldsymbol{r}, t_j)\right)^2 \tag{25}$$

$$D_k(t_i, t_j) = \frac{1}{\mathcal{N}}\int d^3r\left(k_\mathrm{sgs}(\boldsymbol{r}, t_i) - k_\mathrm{sgs}(\boldsymbol{r}, t_j)\right)^2, \tag{26}$$

where $\mathcal{N}$ is a normalization constant so that $D \in [0;1]$. The exponent in Eqs. (25) and (26) is rather arbitrary and hardly influences the final results (Lichtenegger and Miethlinger, 2020).

2.2.2. Recurrence matrix and path

Given a time series of flow fields, $D(t_i, t_j)$ can be computed for each pair of states to obtain the system's distance matrix. Besides this continuous description of similarity, the binary recurrence matrix (Eckmann et al., 1987)

$$R(t_i, t_j; \epsilon) \equiv \Theta(\epsilon - D(t_i, t_j)) \tag{27}$$

is a popular way to discriminate between similar and dissimilar configurations with regard to a reference distance ϵ.

If a time series sampled with steps Δt_rec (the "database") leads to a recurrence matrix where most states have at least recurred once, it is possible to extend it in a meaningful way to much longer durations using a Markov process. We begin at some time step t_l of the database with corresponding fields. For the following step, we take fields from time

$$t_l \rightarrow \begin{cases} t_l + \Delta t_\mathrm{rec} & \text{with prob.} 1 - P_\mathrm{jump} \\ t_{\mathrm{nn}(l)} + \Delta t_\mathrm{rec} & \text{with prob.} P_\mathrm{jump}, \end{cases} \tag{28}$$

i.e. either those from the time directly after t_l or from the time after that past state $t_{\mathrm{nn}(l)}$ which was most similar to t_l according to D. We call this latter state at time $t_{\mathrm{nn}(l)}$ the nearest neighbor to t_l. The probability P_jump to restart from a previous time needs to be chosen with the database size in mind. It is connected to the average length of subsequent steps N_nojump before a jump by

$$P_\mathrm{jump} = \frac{1}{1 + N_\mathrm{nojump}}. \tag{29}$$

We often use a value of N_nojump in the range of half the database size. For more details on the construction of such a recurrence path, we refer the interested reader to our previous publications (e.g. Lichtenegger et al., 2019).

Eq. (28) may be regarded as an iterated method of analogues (Cecconi et al., 2012) and allows to create series of arbitrary length at very little numerical costs. Despite the simplicity of this approximation to the long-term evolution of the system, the resulting sequence has very attractive properties: (i) It consists of a relatively smooth succession of physically valid flow fields (they are taken from the database created with a high-fidelity simulation technique). (ii) It has (approximately) the same spatially resolved mean, variance and higher-order moments as the underlying database (cf. App. A). This can serve as a condition for sufficient database size. Once the leading statistical moments do not change anymore upon increasing database length, recording can be stopped. (iii) Even under circumstances where no clear recurrences might be found (e.g. because of noise), the time-extrapolated series reproduces the correct mean and variance, which explains why it has already proven to work for such scenarios (Abbasi et al., 2020). (iv) If the system under consideration displays any symmetries, they can be enforced in the long-term extrapolation by augmenting the database with a correspondingly transformed series. Then, the recurrence process takes the form

$$t_l \rightarrow \begin{cases} t_l + \Delta t_{\mathrm{rec}} & \text{with prob.} 1 - P_{\mathrm{jump}} \\ \left\{ t_{\mathrm{nn}_i(l)} + \Delta t_{\mathrm{rec}} \quad \text{with prob.} w_i P_{\mathrm{jump}} \right\}_{i=1\ldots N_{\mathrm{db}}}, \end{cases} \tag{30}$$

where jumps can lead to any of the N_{db} databases with weights w_i. For the example of a system with reflection symmetry in one direction, we would have the initial and the mirrored database with equal weights $w_1 = w_2 = 0.5$.

Eq. (30) can also be used to account for gradual changes in the dynamics. In this work, we consider flows at different inlet velocities $u_{\mathrm{low}} \leqslant u \leqslant u_{\mathrm{high}}$. Having available databases corresponding to u_{low} and u_{high}, we can attempt to form a superposition by adjusting the weights w_i such that the desired inlet velocity is obtained. These weights may vary with time such that a time-dependent inlet condition can be realized.

2.2.3. Long-term simulations with rCFD

If the velocity field of a turbulent flow is time-extrapolated as explained above, it is straight-forward to investigate bubble motion according to Eq. (20). The velocity field is available without further computations, and the velocity fluctuations $\boldsymbol{v}_{\mathrm{fluc}}$ can be calculated e.g. via the sub-grid-scale kinetic energy. Indicating quantities obtained from the recurrence process with a superscript (rec), Eq. (20) turns into

$$\frac{d}{dt}\boldsymbol{r}_i = \boldsymbol{u}_{\mathrm{f}}^{(\mathrm{rec})}(\boldsymbol{r}_i) + \boldsymbol{v}_{\mathrm{t}} + \boldsymbol{v}_{\mathrm{fluc}}\left(k_{\mathrm{sgs}}^{(\mathrm{rec})}\right). \tag{31}$$

In order to solve Eq. (31) numerically, a time step $\Delta t_{\mathrm{bubble}}$ needs to be chosen that is sufficiently small to resolve both temporal and spatial variations of the velocity and kinetic energy fields, which limits its size to the same value as for Eq. (20). If one wants to use a larger step size, one needs to tame the rapid fluctuations of a turbulent flow. To this end, we introduce the displacement field

$$\dot{\boldsymbol{d}}(\boldsymbol{r}, t) \equiv \frac{1}{\Delta t_{\mathrm{bubble}}} \sum_i g(|\boldsymbol{r} - \boldsymbol{r}_i(t)|)(\boldsymbol{r}_i(t + \Delta t_{\mathrm{bubble}}) - \boldsymbol{r}_i(t)), \tag{32}$$

which corresponds to the bubble velocity *averaged along the trajectories*. We interpret the displacement field as a combination of velocity-based motion and discrete cell-to-cell shifts (Pirker and Lichtenegger, 2018) uniting the benefits of each approach: It contains finite-time displacements eliminating the need to resolve the strong curvature of the turbulent velocity field, but it still has the geometric interpretation of a vector field, which is useful to interpolate it in empty cells.

Eq. (32) can be evaluated easily if bubble positions are recorded with a sampling step $\Delta t_{\mathrm{bubble}}$, and can be time-extrapolated in the same way as other flow fields. Since it already contains the effect of the terminal rising velocity, the bubble EOM (31) turns into

$$\frac{d}{dt}\boldsymbol{r}_i = \dot{\boldsymbol{d}}^{(\mathrm{rec})}(\boldsymbol{r}_i) + \boldsymbol{v}_{\mathrm{fluc}}\left(k_{\mathrm{sgs}}^{(\mathrm{rec})}\right), \tag{33}$$

which can be solved safely with a larger time step. If the fluctuations $\boldsymbol{v}_{\mathrm{fluc}}$ are merely a small correction over convective transport, no specific treatment for using a larger value of $\Delta t_{\mathrm{bubble}}$ is necessary. Otherwise, one could compute the variance of displacement analogously to Eq. (32) to approximate $\boldsymbol{v}_{\mathrm{fluc}}$.

As already pointed out in previous investigations (Abbasi et al., 2020), passive transport may be calculated on a significantly coarser mesh than that employed for the solution of the momentum and pressure equation. It is not very farfetched to assume the same for weakly coupled transport as in the present study. Hence, we either map the velocity field from the LES mesh to a coarser one C for the rCFD simulations, or we evaluate Eq. (32) with lower resolution. In either case, the loss of fine-scale information needs to be accounted for in terms of an effective diffusivity. We employ Germano's et al. (Germano et al., 1991; Germano, 1992) identity for the consecutive application of two filters for the residual stress, and find

$$k_{\mathrm{eff}} = \langle k_{\mathrm{sgs}} \rangle_{\mathrm{C}} + \frac{1}{2}\langle \boldsymbol{u}_{\mathrm{f}} \cdot \boldsymbol{u}_{\mathrm{f}} \rangle_{\mathrm{C}} - \frac{1}{2}\langle \boldsymbol{u}_{\mathrm{f}} \rangle_{\mathrm{C}} \cdot \langle \boldsymbol{u}_{\mathrm{f}} \rangle_{\mathrm{C}}, \tag{34}$$

where $\langle . \rangle_{\mathrm{C}}$ indicates filtering with respect to the coarser mesh. The full velocity fluctuations k_{eff} on C consist of the LES sub-grid-scale kinetic energy k_{sgs} and the fluctuations of the LES velocity evaluated on C. Therefore, we use $\boldsymbol{v}_{\mathrm{fluc}}\left(k_{\mathrm{eff}}^{(\mathrm{rec})}\right)$ to picture bubble dynamics at a lower resolution.

3. Case and simulation setup

During continuous casting of steel, a double-jet of liquid steel laden with argon bubbles enters a container (the mold) with an open top where slag separates steel from air (Thomas, 2018). Various publications have addressed this type of problem (e.g. Chen et al., 2019; Chen et al., 2019; Li et al., 2021; Liu et al., 2019; Jin et al., 2018; Puttinger and Saeedipour, 2022; Trang et al., 2019; Wu et al., 2019). However, all of them are plagued by the jets' inherent multi-scale nature, which prevents the efficient simulation of long-term transport.

3.1. LES

Our case setup of liquid steel carrying argon bubbles through a submerged entry nozzle (SEN) into the mold was inspired by the works of Cho et al. (2014) and Javurek and Wincor (2020). The domain displayed in Fig. 1 was discretized into $N_{\mathrm{cell}}^{(\mathrm{LES})} = 3.075 \cdot 10^6$ cells with side lengths $\Delta x_{\mathrm{cell}} \approx 3 - 5\,\mathrm{mm}$ in the SEN and the jet regions. The dimensions of the nozzle port and the mold are provided in Table 1.

We assumed a liquid density of $\rho_{\mathrm{f}} = 7000\,\mathrm{kg/m^3}$ and viscosity of $\nu_{\mathrm{f}} = 1 \cdot 10^{-6}\,\mathrm{m^2/s}$, which were in the range of values typically found in publications on continuous casting of steel (e.g. Chen et al., 2019; Huang and Thomas, 1998). Notably, our choice of ν_{f} corresponded to conditions far from solidification, where a massive increase of viscosity takes place. Depending on the composition of the liquid steel under consideration, this would imply temperatures above 1520°C (Miettinen and Howe, 2000; Sołek et al., 2012). Besides any temperature dependence, we also neglected the variation of viscosity with the local shear rate even though shear thinning in liquid steel has been clearly documented (Sołek et al., 2012). The density of argon bubbles was $\rho_{\mathrm{b}} = 0.5\,\mathrm{kg/m^3}$. To keep their number in a reasonable range, we chose a diameter of $d_{\mathrm{b}} = 5$. Based on these values and the findings of Javurek and Wincor, 2020; Szekely, 2012, we estimated a terminal rising velocity of $v_{\mathrm{t}} = 0.22$ m/s. Furthermore, we carried out a case variation with smaller bubbles of $d_{\mathrm{b}} = 1.5\,\mathrm{mm}$, for which we set $v_{\mathrm{t}} = 0.18\,\mathrm{m/s}$ (cf. Section 4.5).

We stress that a notable amount of uncertainty is connected to the determination of v_{t}. Force correlations from rigid particles may be used only for relatively small bubbles, because larger ones deform and exhibit more complicated trajectories (Ford and Loth, 1998). This is a consequence of surface tension and can be approximately accounted for with Weber number dependent drag coefficients (Chen et al., 2019; Kuo and Wallis, 1988). Alternatively, the terminal rising velocity may be measured. Due to their similar kinematic viscosities, results from experiments with water carry over to liquid steel for not-too-large bubbles to some extent. Indeed, our choice of v_{t} extracted from such measurements agreed with the range of values reported by Zhang et al., 2006 where several force correlations were compared for the case of liquid steel.

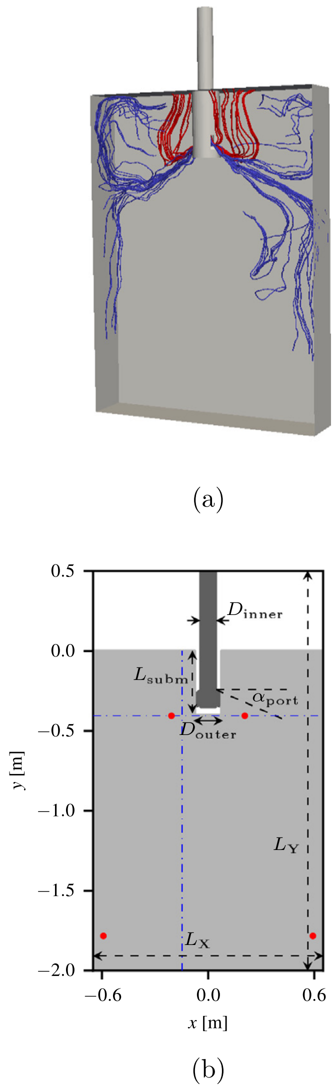

Fig. 1. Simulation geometry. (a) A sketch of the domain illustrates how bubbles (red) and fluid (blue) followed a few selected streamlines. Bubbles left the box through the top surface, while liquid flowed through the bottom plane. (b) A cross section at $z = 0$ provides more details about the geometry. The darker region indicates the submerged entry nozzle (SEN) through which material entered the mold shown in lighter gray. Values for the various parameters can be found in Table 1. The extent in z direction and the cross section of the SEN port are not indicated. The red dots represent the probing points (cf. Figs. 3 and 4), and the line plots of Fig. 15 are marked in d.ash-dotted blue.

Table 1
Dimensions of the computational domain. The parameters are illustrated in Fig. 1.

Domain parameters	
L_X	1300 mm
L_Y	2500 mm
L_Z	125 mm
D_{inner}	85 mm
D_{outer}	150 mm
A_{port}	$80 \times 85\,mm^2$
α_{port}	-30°
L_{subm}	400 mm
probe points	$(\pm 200, -420, 0)$ mm
	$(\pm 600, -1800, 0)$ mm
probe lines	$(x, -410, 0)$ mm
	$(-150, y, 0)$ mm

Altogether, three LES cases were carried out: one at low inlet velocity $u_{low} = 1.6\,m/s$, one at high inlet velocity $u_{high} = 3.2\,m/s$, and one with a linear increase from u_{low} to u_{high}. The two velocities corresponded to $Re = 136\,000$ and $Re = 272\,000$ with the SEN diameter taken as characteristic length scale. In all simulations, we set a bubble concentration of $\alpha_b \approx 0.075$ in the SEN.

For the sake of simplicity, we adapted the treatment of the top boundary. There is a slag layer with a free surface of air above it in an actual continuous casting plant, which would necessitate a multi-fluid-phase description along with the dispersed bubble phase. Hence, we put a fixed wall on top of the liquid steel in our simulations. We stress that this does not affect the conclusions of our investigation but would only have made the case setup more cumbersome.

We solved Eqs. (1), (20) and (24) using the PISO algorithm implemented in CFDEMcoupling (Goniva et al., 2012) together with the DEM code LIGGGHTS (Kloss et al., 2012). Time steps were small enough to keep the Courant number below 0.6 and can be found in Table 2. The second-order central difference scheme was applied to gradient, convection and diffusion terms, and for transient parameters, Euler first-order discretization was used.

After equilibration, validation data were recorded over durations of $\tau_{val} = 20\,s$ for the low-velocity case and $\tau_{val} = 30\,s$ for the high and the time-varying velocity.

3.2. rCFD

We employed rCFD's resilience against grid coarsening (Abbasi et al., 2020) and carried out all time-extrapolated simulations on a mesh with only $N_{cell}^{(rCFD)} = 350\,000$, which corresponded to about 11% of the LES value and amounted in roughly twice as large cell side lengths. Despite the bigger volumes, instances occurred during the rCFD runs, where bubbles arrived at a cell c at time t_i that had not been occupied during LES so that $\dot{\boldsymbol{d}}(\boldsymbol{r}_c, t_i)$ was not defined. We circumvented this problem by interpolating $\dot{\boldsymbol{d}}(\boldsymbol{r}_c, t_i)$ between the three nearest, filled cells if such where located in the first few adjacent layers. Otherwise, the value of the displacement field in empty cells was set to the time-averaged fluid plus the terminal rising velocity at this location.

Compared to LES, we used significantly larger time steps Δt_{CFD} (time interval to assign a new velocity or displacement to a bubble depending on its current location), Δt_{bubble} (time interval for bubble motion in Eq. (20); smaller than Δt_{CFD} to account for bubble-wall contacts) and Δt_{rCFD} (sampling step of the recurrence process). The values for the various simulations are provided in Table 3.

We carried out simulations over the same duration as for the LES cases. Since rCFD involves the stochastic creation of the recurrence path, we ran each rCFD case three times and report the averaged values in Section 4. However, the results from each run differed only in minor details if any deviations could be found at all.

4. Results

We first discuss the dynamics of the flow obtained from LES at low and at high inlet velocity. We explain the equilibration procedure and the choice of database size. Then, we present the results

Table 2
Time steps for LES for the low, high and time-dependent inlet velocity.

	u_{low}	u_{high}	$u(t)$
Δt_{bubble}	$5 \cdot 10^{-4}\,s$	$2.5 \cdot 10^{-4}\,s$	$2.5 \cdot 10^{-4}\,s$
Δt_{CFD}	$5 \cdot 10^{-4}\,s$	$2.5 \cdot 10^{-4}\,s$	$2.5 \cdot 10^{-4}\,s$

Table 3
Time steps for the rCFD simulations. For the time-dependent inlet velocity, different sampling steps depending on the current database were used.

	u_{low}	u_{high}	$u(t)$
Δt_{bubble}	$2.5 \cdot 10^{-3}$ s	$2.5 \cdot 10^{-3}$ s	$2.5 \cdot 10^{-3}$ s
Δt_{CFD}	$2.0 \cdot 10^{-2}$ s	$1.0 \cdot 10^{-2}$ s	$1.0 \cdot 10^{-2}$ s
Δt_{rCFD}	$2.0 \cdot 10^{-2}$ s	$1.0 \cdot 10^{-2}$ s	$1.0 \cdot 10^{-2}$ s and $2.0 \cdot 10^{-2}$ s

of our fast rCFD calculations and highlight the importance of a sufficient amount of information contained in the databases. We answer the question if an extremely noisy, structureless distance matrix implies a stochastic process without memory, and we tackle the issue of flow conditions different from those in the databases. Finally, we discuss certain case variations to demonstrate the generality of our approach.

4.1. Full-CFD analysis of the flow dynamics

We let our simulations equilibrate in a two-step procedure before we could safely start sampling data for time-extrapolation. First, we carried out single-phase LES until the total kinetic energy in the system had converged such that it fluctuated around a fixed value. Then, we began inserting bubbles. Besides the time it took for them to spread throughout the domain, their presence also affected the flow dynamics mainly due to the displaced volume. Fig. 2 shows that after approximately 12.5 s, the bubble hold-up was in equilibrium and oscillated only weakly around its mean. We concluded that data sampling was permissible starting from $t_{equil} = 15$ s.

Next, we had to determine a sufficient duration for recording our database. On the one hand, it needed to be large enough to contain the essential flow dynamics, while on the other hand, it should be as small as possible to reduce loading times and not exceed the available RAM for the simulations. To estimate a reasonable length of the time series, we monitored the velocity and its temporal average in the jet regions at $(\pm 0.2\,\mathrm{m}, -0.42\,\mathrm{m}, 0.0\,\mathrm{m})$ and close to the bottom at $(\pm 0.6\,\mathrm{m}, -1.8\,\mathrm{m}, 0.0\,\mathrm{m})$. Once the mean values had converged, we could hope to have covered the relevant dynamics of the system. Notably, the converged mean values should satisfy the symmetries of the flow, i.e. left–right reflection symmetry in the present case. It can be seen in Fig. 3 that 2.5 s of the low-velocity flow (starting from t_{equil}) were enough to obtain good approximations for the mean velocity field. A slight asymmetry was present close to the bottom, but it would have taken much longer until it averaged out.

As pointed out in Section 1, the type of flow under investigation can exhibit very slow, "wobbling" modes where one jet points more downwards than the other and vice versa. While this effect was rather weak for the low inlet velocity, it was much more pronounced for the higher one. Fig. 4 shows that the temporal averages had by far not converged after the observation period of 5 s. It would have taken such a long sampling time to fully represent the dynamics that (i) the database size would have exceeded any available RAM and (ii) the long CPU time for recording would have rendered our subsequent fast simulations pointless. Within a short monitoring duration corresponding to a feasible database size, the low-velocity flow reached its dynamic equilibrium, while the high-velocity case did not explore all configurations dictated by symmetry considerations as can be

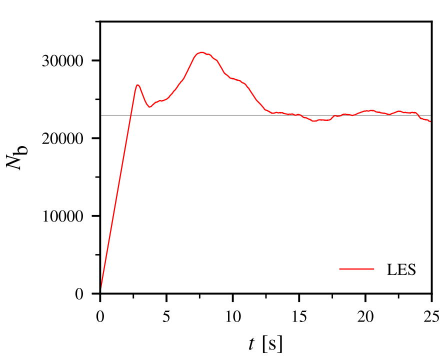

Fig. 2. Total number of bubbles N_b for LES at low inlet velocity. After a steep, initial increase, N_b exhibited some fluctuations before approaching the relatively constant equilibrium value (shown as thin grey line).

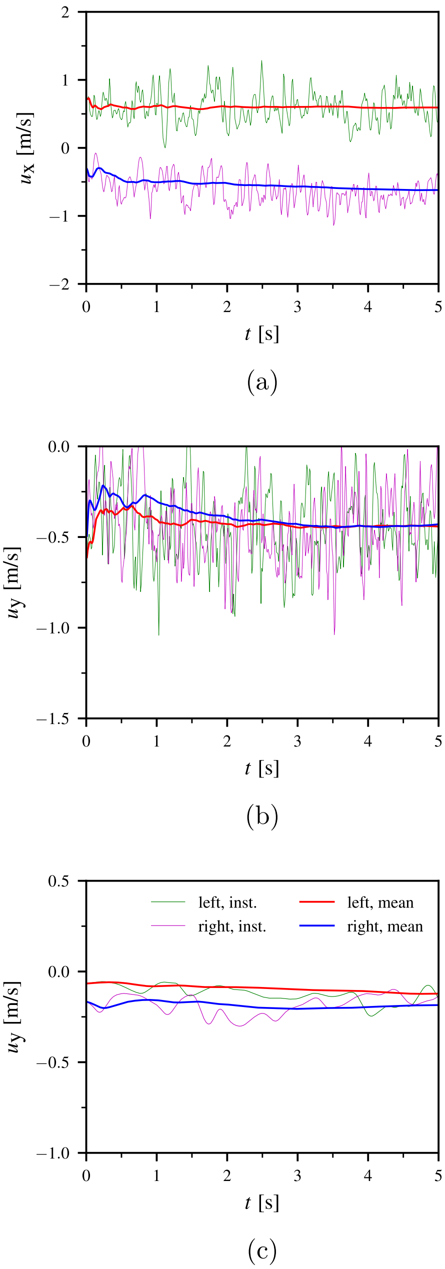

Fig. 3. Velocity probe values and their averages for the low inlet velocity. Even though the velocity varied strongly and rapidly, the running temporal mean converged quickly. In the jet regions, (a) the horizontal components of the means reached opposite values and (b) the vertical components (almost) identical values after about 2.5 s. Notably, the vertical mean values close to the bottom (c) were slightly different indicating a weak asymmetry of the flow over the observation time.

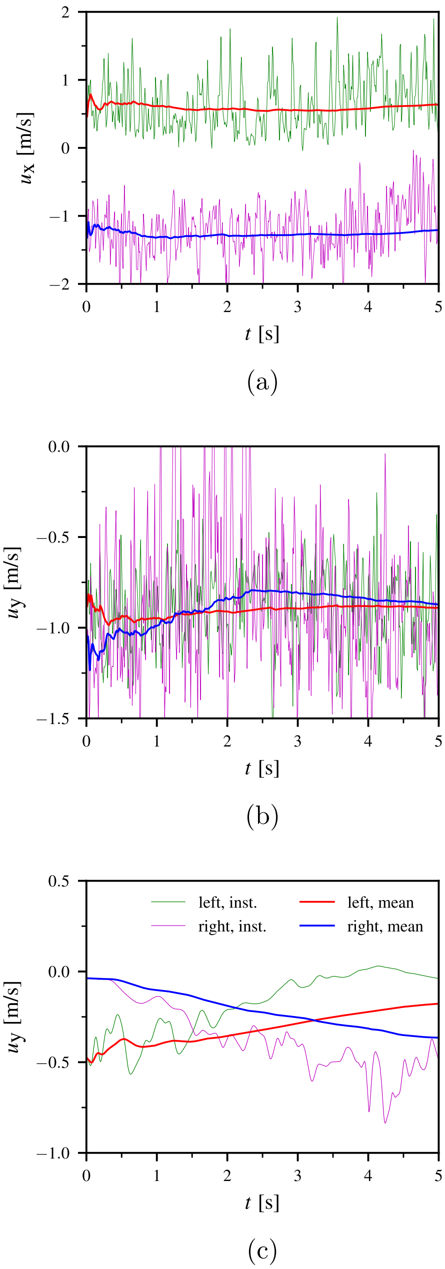

Fig. 4. Velocity probe values and their averages for the high inlet velocity. In the jet region (a) and (b), the mean values varied only slowly after 5 s but had different magnitudes in the two jets. Close to the bottom (c), the mean values differed from each other and they still changed significantly even after 5 s. This corresponded to a slow wobbling motion of the whole system.

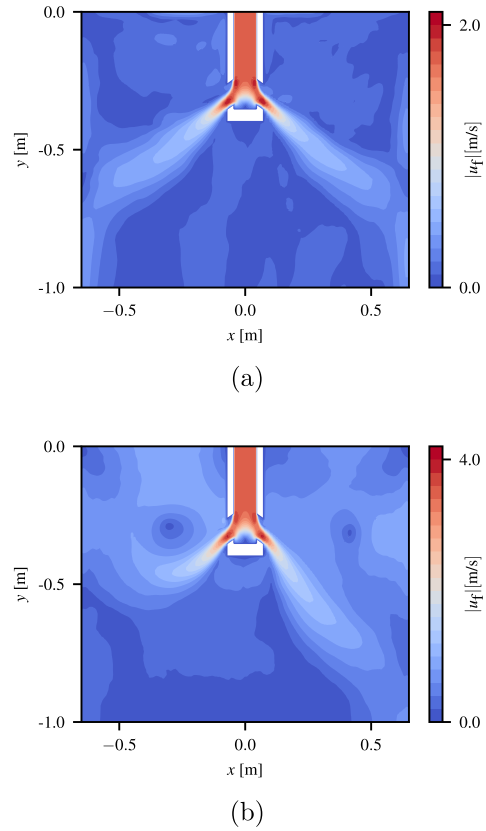

Fig. 5. Velocity fields averaged over 2.5 s. While the low-velocity case (a) showed a high degree of left–right symmetry, the high-velocity case (b) was clearly asymmetric with the right-hand jet pointing further downwards than the left-hand one. Note the different scales.

seen in Fig. 5. We reassure the worried reader that we deal with this problem in Section 4.3.

Even though the flow fluctuated rapidly and, at least for the low-velocity case, the mean had converged at all investigated probing points, this did not mean that recurrences of large spatial extension (and much less of system-wide nature) had occurred. The distance matrices in Fig. 6, which were calculated over the jet region, contain hardly any structures corresponding to reappearing states. Most encountered configurations had a very similar, large distance from all others, which is typical for high-dimensional dynamics. Notably, a long-term drift can be seen for the high-velocity case in Fig. 6b, which is connected to the low-frequency oscillation of the wobbling jet.

4.2. rCFD for fixed, low inlet velocity

The utter absence of recurrences in the distance matrices of the flow might cast doubts on the appropriateness of our time-extrapolation approach being based on the method of analogues (Cecconi et al., 2012). However, as stated in Section 2, rCFD produces a time-series with (approximately) the same statistical moments as the underlying database even if no pronounced recurrences are present. The extrapolated time series might contain rather abrupt variations, but this would be the case for turbulent flows anyway. For this reason, previous rCFD studies of species transport under turbulent conditions (Abbasi et al., 2020; Abbasi et al., 2020), which faced the same issue of structureless distance matrices, could achieve reasonable accuracy. Unfortunately, these investigations only reached speed ups of 120 and 15 compared to the underlying LES because the rapid fluctuations of the velocity fields limited the time step sizes in the solution procedure of the passive transport equations. In principle, the motion of discrete bubbles in the present case was impacted by the same limitation as continuous field representations. However, the time-averaged bubble volume fraction fields displayed in Fig. 7 demonstrate that this problem could be overcome with the use of the displacement instead of the velocity field. While velocity-field-based rCFD with large time steps failed to reproduce LES data (the ground truth), rCFD calculations built upon the displacement field Eq. (32) gave results in close agreement with LES. The overall bubble hold-up was less affected by the choice of transport mechanism. Fig. 8 indicates that both velocity- and displacement-field-based rCFD led to values almost within the standard deviation around the time-averaged LES result, i.e. to errors on the order of a few percent.

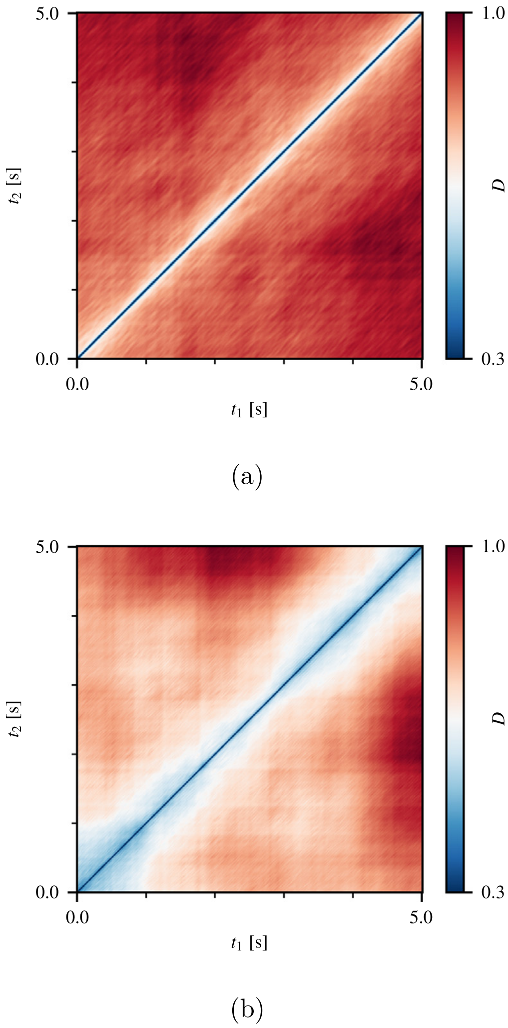

Fig. 6. Distance plots for (a) low and (b) high inlet velocity. Apart from the trivial main diagonal, no pronounced structures are present. Only weak hints of short segments parallel to the main diagonal can be seen. In (b), a clear drift towards larger distances for longer separations (darker red regions at the borders of the plots) indicates a slow, underlying shift of the dynamics connected to low-frequency oscillations of the jets. Distances for both cases have been normalized to $[0;1]$, hence each plot needs to be interpreted separately with regard to its color distribution.

Notably, it was important to include dispersion effects even though the displacement field already contained some of the influence of the rapidly varying velocity field. Nevertheless, it represented the *average* displacement over one time step of all bubbles starting from the same cell. In addition, turbulent fluctuations ($\boldsymbol{v}_{\mathrm{fluc}}$ in Eq. (33)) took care that bubbles which were located in the same cell at a certain time were displaced to slightly different positions after one step. Such a mechanism was important to prevent the creation of artificial high-concentration spots due to recirculation. It can be seen in the LES results in Fig. 7a that such regions existed and could be reproduced if fluctuations were retained for bubble transport (cf. Fig. 7b), but failure to account for dispersion led to erroneous enlargement of these spots (cf. Fig. 7c). As a consequence, not only did the distribution of bubbles in the domain come out wrong, but the total bubble number in the domain also increased (cf. Fig. 8).

We conclude that it is possible to perform large-step rCFD calculations even for rapidly fluctuating flows as long as one uses the displacement field and includes the effect of turbulent dispersion. A notable speed up of about 610 compared to the LES runtime was reached even though rCFD was carried out with only eight threads and LES ran on 32. The computational costs required to simulate 1 s of process time with LES and with rCFD are provided in Table 4.

4.3. rCFD for fixed, high inlet velocity

As explained in Section 4.1, the flow dynamics at high inlet velocity was significantly more complicated than at lower values because very slow but rather pronounced jet oscillations emerged. This made it completely unfeasible to record even a single pseudo-period. However, a short time series of flow fields would likely have an asymmetric temporal average, and consequently the long-term bubble distribution would be asymmetric, too. Of course, the long-term distribution from LES without any time-extrapolation should be symmetric in accordance with the problem's boundary conditions. This can be seen in Fig. 9a, where the averaged bubble volume fraction over 30 s of an LES run is displayed. However, the rCFD result from a time-extrapolated 2.5 s database in Fig. 9b is clearly asymmetric and does not match the LES findings. While bubbles on the right-hand side were transported strongly downwards, those on the left-hand side remained in the upper part of the domain and exited the mold at the top. As a consequence, the total number of bubbles in the system was not obtained correctly, either. Fig. 10 shows that after the initial rise from an empty configuration, the bubble hold-up surpassed the average LES value significantly. The downwards pointing jet drove a large fraction of the inserted bubbles down into the mold where some of them moved through the outlet, while many others resided some time before making their way up again due to buoyancy. This caused the total number of bubbles to be unrealistically high. However, if the database was augmented with its mirrored counterpart and sequences of flow fields were drawn from both of them, none of the jets transported a significant number of bubbles too far down except very close to the walls. Hence, their overall number remained smaller and in good agreement with the LES value. Similarly, the time-averaged spatial bubble concentration in Fig. 9c improved significantly with the augmented database as compared to the rather poor result of the un-symmetrized time series in Fig. 9b. We achieved a speed up of approximately 500, which was slightly lower than for the low-velocity case because of the larger number of bubbles in the domain with higher inlet velocity. Table 4 shows that runtimes both for LES and for rCFD increased more than twice compared to the low-velocity case because twice as many steps had to be taken and more bubbles were present.

Given the very noisy, almost structureless distance matrices Figs. 6a and b, we might question the importance of a reasonable choice of recurrence path under turbulent conditions. Since all states had a large distance from all others, the recurrence path consisted of flow field intervals chained in a completely random fashion. Hence, we might think one step further and ask if we could take random, single steps, which would correspond to a process without any memory. If such a strategy was found permissible, one could describe bubble transport with only two fields: their mean displacement and a stochastic contribution of the fluctuations around the mean. The averaged bubble volume fraction field in Fig. 9d obtained from a random sequence of single steps in the symmetry-extended database pair and the total number of bubbles in the domain provided in Fig. 10 seem to support this hypothesis. However, closer inspection of the spatial bubble concentration in Fig. 9d reveals that too few bubbles moved downwards into the mold, whereas a slightly elevated number created vortex-like structures in front of the two outlets from the SEN. While the visual discrepancy from the LES result and rCFD calculation with finite-length intervals in Figs. 9a and c was actually not very large,

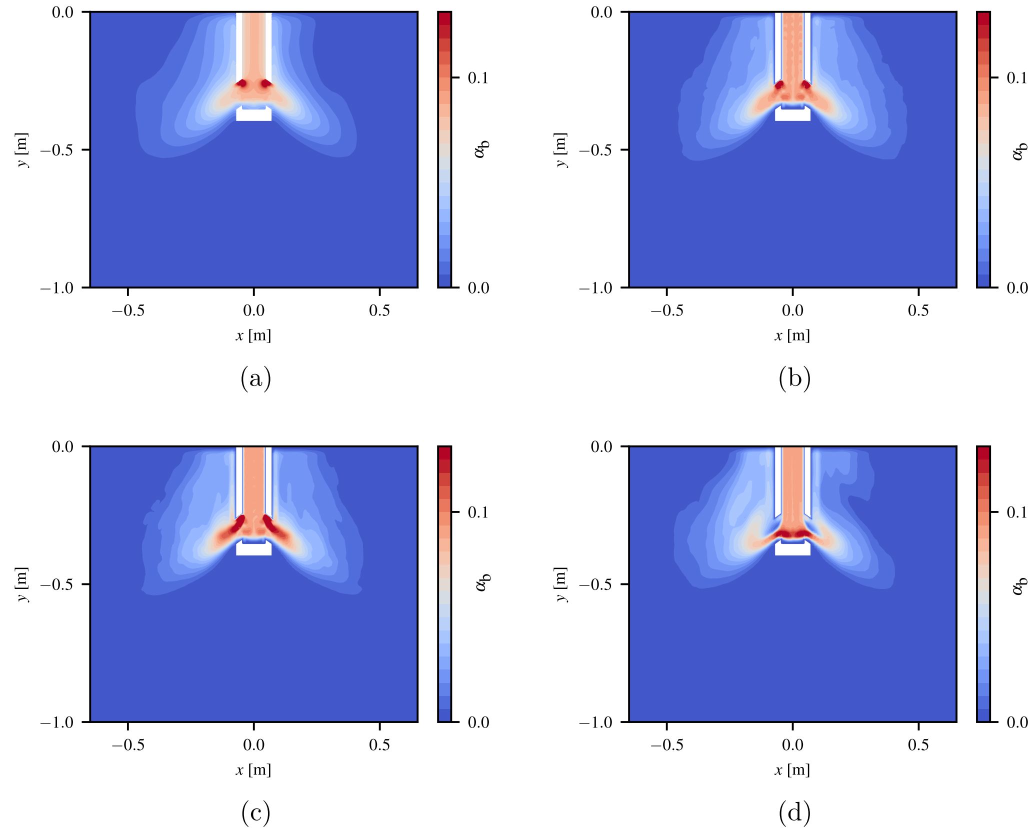

Fig. 7. Time-averaged bubble volume fractions at low inlet velocity. The LES result (a) was best reproduced by the displacement-based rCFD calculation (b). A high bubble concentration region was located at the upper edge of the outlet from the SEN, where recirculation occurred. Without the influence of fluctuations (c), the recirculation regions extended too far from the SEN. Velocity-field-based rCFD (d) with the same time step size failed to predict a reasonable bubble distribution because bubbles could not follow the strong curvature of the velocity field lines, which caused accumulation at the lower part of the SEN.

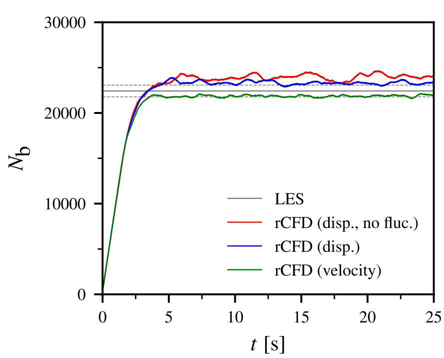

Fig. 8. Total number of bubbles N_b for different rCFD settings with low inlet velocity. Velocity- and displacement-based (the latter both with and without fluctuations) rCFD led to bubble hold-ups almost within the standard deviation of the LES result (dashed gray lines around the solid gray line). If turbulent dispersion effects were neglected, N_b increased slightly.

Table 4
Simulation runtimes per second process time. 32 threads were used for LES and eight for rCFD. Equilibration and preprocessing times (costs to generate databases) are not included.

	LES	rCFD
u_{low}	24333 s	40 s
u_{high}	51594 s	104 s

a more quantitative analysis of the bubble behavior turned out to be less forgiving. The number of bubbles leaving the system through the bottom outlet provided in Table 5 differed massively between the various rCFD settings. Only the case with a symmetry-extended database could predict a similar value as LES. Notably, the recurrence path consisting of random single steps failed with a relative error of more than 40%.

We can conclude that a rather uniform distance matrix does not imply a stochastic process without memory. Strong temporal correlations may still be present and have a major influence, which is proven by the fact that rCFD simulations with finite-length intervals of flow fields outperformed those with random sequences of single steps by far. Therefore, we are not overly optimistic that this process could be described with only the bubble mean displacement (or velocity) field and its variance.

4.4. Statistical interpolation for different inlet velocities

In the previous sections, it was shown that even short time series of only 2.5 s length contained the relevant dynamics of a turbulent flow under fixed boundary conditions such that they could be time-extrapolated to arbitrarily long durations. However, was the information of two (or more) databases corresponding to not too different conditions also sufficient to picture the properties of a flow in between these conditions? In the present case, we successfully time-extrapolated flow fields corresponding to a low and a high inlet velocity u_{low} and u_{high}. Next, we attempted to obtain the dynamics of a flow with an inlet condition $u_{low} \leqslant u(t) \leqslant u_{high}$. For the sake of simplicity, we considered a linear function

$$u(t) = u_{low} + \frac{t}{\tau}(u_{high} - u_{low}) \qquad 0 \leqslant t \leqslant \tau \tag{35}$$

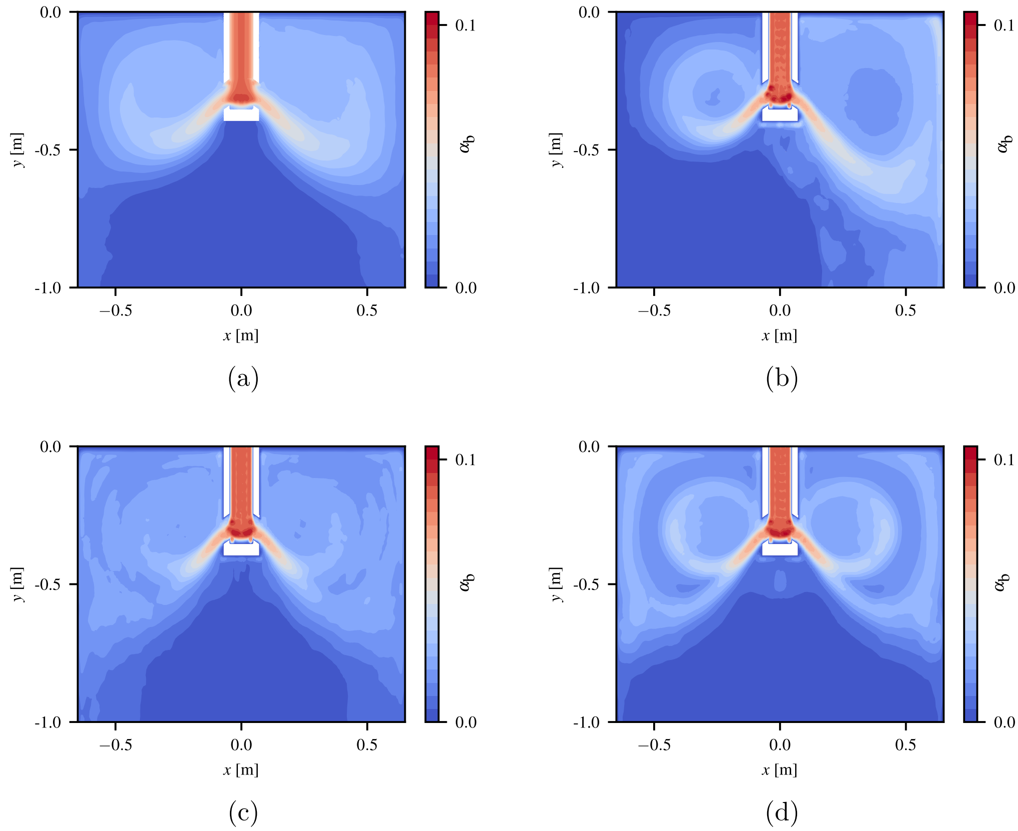

Fig. 9. Time-averaged bubble volume fraction fields at high inlet velocity. The LES result (a) shows a high degree of left–right symmetry with most of the bubbles located in the upper region and fewer going downwards. rCFD built upon a single, short database (b) could not reproduce this pattern because the right-hand jet moved too many bubbles downwards and the left-hand jet too few. Extension with a second, mirrored database (c) gave results in much better agreement with LES (a). A randomly shuffled recurrence path without any temporal correlation (d) led to a distribution with slightly too many bubbles in the upper part of the domain and too few moving downwards but in qualitative agreement with the reference field.

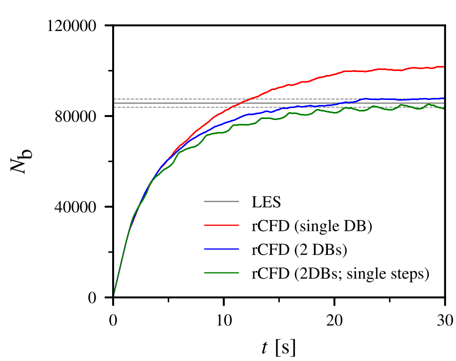

Fig. 10. Total number of bubbles N_b for different rCFD settings with high inlet velocity. While rCFD with a single database overpredicted the hold-up, the use of a symmetry-extended, second database allowed for a significantly more accurate result that deviated from LES only slightly. A recurrence path consisting of single steps randomly picked from the database and its mirrored counterpart found a total number of bubbles with similar accuracy.

Table 5
Number of bubbles leaving the domain through the bottom outlet per second. Values have been obtain by fits to the last 15 s of the simulations when flow conditions had stabilized.

	$\dot{n}_{\mathrm{bottom}}$	rel. error
LES	493.4	–
single DB	387.7	−0.21
symmetry-ext. DBs	463.3	−0.06
random single steps	289.8	−0.41

over a duration of $\tau = 30\,\mathrm{s}$. We carried out a corresponding LES to generate reference data and an rCFD simulation built upon the two databases (and their mirrored extensions) from the fixed inlet velocities. At the beginning of the simulation, flow fields were drawn mainly from the low-velocity databases, while at the end of the run, mainly the high-velocity databases were used. In between, fields were taken from both configurations. Even though the results for bubble hold-up and spatial distribution shown in Figs. 11 and 12 did not reach the same level of accuracy as those in Sections 4.2 and 4.3, we regard them nevertheless as acceptable. Given the admitted crudeness of this procedure, we find it even surprising that some qualitative features could be reproduced if the results were interpreted properly. As noted in previous work (Lichtenegger et al., 2019), the statistical interpolation technique implies that simulation output might need to be filtered to reduce the noise due to rapid jumps between databases. Under these circumstances, the time-dependent bubble hold-up obtained with rCFD agreed fairly well with that from LES. Notably, it was not simply given by the instantaneous, weighted average of the equilibrium values corresponding to the low and high inlet velocity because it took some time until the changes in the transport behavior had developed. In Fig. 11, this is most obvious for $t = \tau$ where LES and rCFD both led to approximately the same value significantly lower than that obtained for fixed high inlet velocity shown in Fig. 10. After a few more seconds corresponding to the mentioned delay, N_b would have risen to this level for both LES and rCFD. Hence, the statistical interpolation technique captured more of the dynamics than a simple, linear superposition of the database averages, which justifies its use at least as a rough approximation. However,

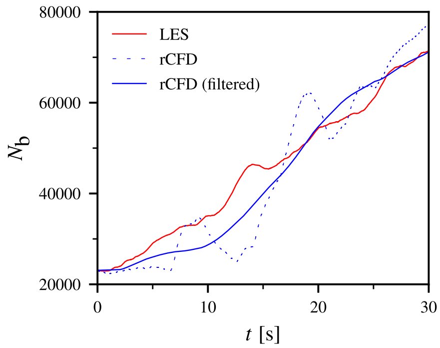

Fig. 11. Total number of bubbles N_b for linearly increasing inlet velocity. LES predicted a more or less monotonous rise, whereas the statistical interpolation technique of rCFD led to a more complicated curve with pronounced peaks. However, temporal filtering produced a result in rough agreement with that from LES.

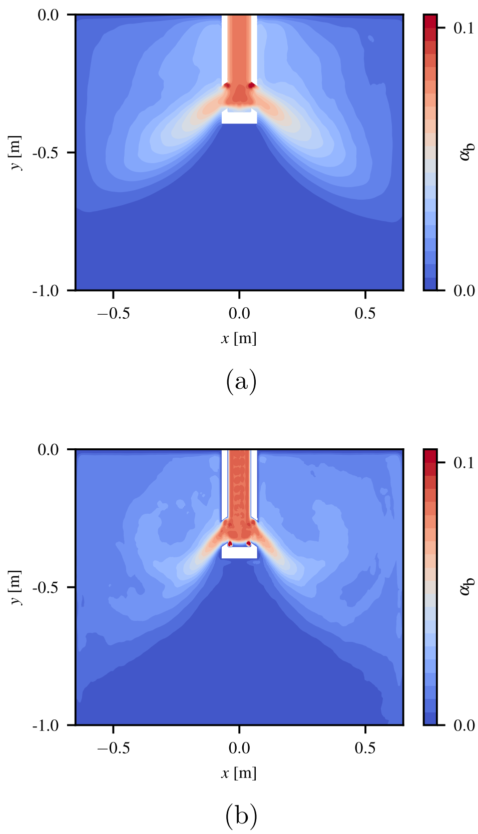

Fig. 12. Time-averaged bubble volume fraction fields over the ramp duration of 30 s. As expected, the field obtained from LES lay between the extreme cases of low and high inlet velocity. rCFD could reproduced some qualitative features not too close to the SEN outlet, but failed to capture all details like the exact angle of the bubble stream or local accumulation points.

one has to be aware that it cannot reproduce all details of highly non-linear flow behavior. Fig. 12 demonstrates that while the penetration depth of bubbles into the mold came out in qualitative agreement, details like bubble stream angle or accumulation points differed between LES and rCFD.

4.5. Selected case variations

The results presented so far demonstrate the capability of rCFD to capture the most relevant aspects of bubble transport in a non-trivial flow. We substantiate that these findings are not connected to the specifics of the chosen case setups, but may be assumed to hold more generally. To this end, we investigate the influence of (i) bubble size and (ii) the choice of database during the low-frequency oscillation cycle observed at high inlet velocities. Regarding (i), due to their lower terminal rising velocity, smaller bubbles follow the fluid flow more easily than larger ones, which makes them more sensitive towards velocity fluctuations and could pose a challenge for rCFD. Hence, we contrasted the behavior of 5 mm bubbles studied in the previous sections with that of 1.5 mm bubbles at the same inlet volume fraction. As expected, Fig. 13 shows that smaller bubbles penetrated slightly farther into the mold and gave rise to a smaller accumulation region at the upper edge of the SEN than larger ones. The same behavior was observed by LES and by rCFD with a similar accuracy as for the case of larger bubbles. Notably, the volumetric hold-up increased significantly. Due to their lower terminal rising velocity, smaller bubbles remained in the domain for a longer duration. Fig. 14 demonstrates that this effect was captured with high accuracy by rCFD.

While the unproblematic simulation of smaller-sized bubbles did not come as a big surprise, issue (ii) was connected to a larger amount of uncertainty. If recurrent dynamics changes slowly over time and only a short duration can be captured in a database, how important is the specific choice when to start sampling? In the current case, slow jet oscillations would cause more or less asymmetric configurations which we balanced by symmetrizing the database. On the one hand, one might assume that less asymmetric

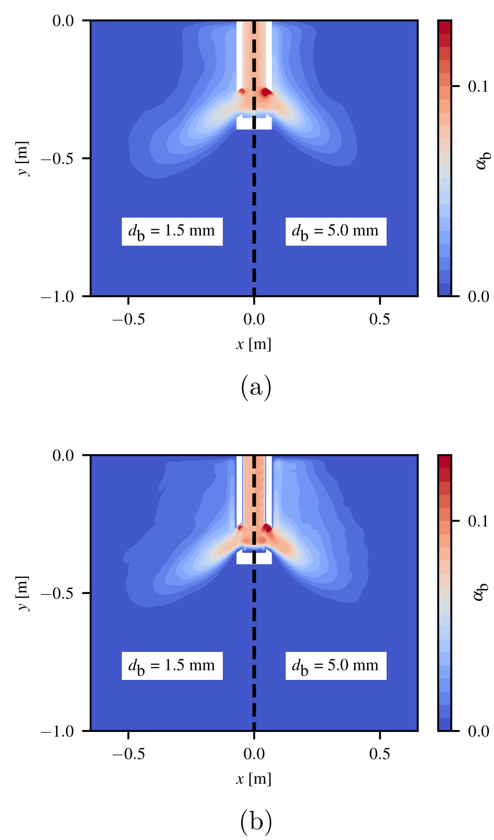

Fig. 13. Time-averaged bubble volume fraction fields for different bubble sizes at low inlet velocity. LES results (a) confirmed the rCFD prediction (b) that smaller bubbles which rise more slowly were transported farther into the mold before ascending to the surface. The left-hand side of both plots corresponds to simulations with smaller bubbles while the right-hand side stems from calculations with the original diameter (cf. Section 4.2).

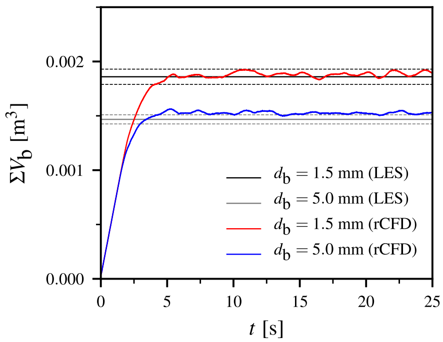

Fig. 14. Total volumetric hold-up for large and small bubbles. With the same inlet condition, a larger amount of smaller bubbles (not only with regard to their number but also to their total volume) was contained within the simulation domain. For both diameters, the rCFD result agreed very well with LES.

flow states can be symmetrized more easily, while on the other hand, strongly asymmetric fields might pose a better representation of the long-term evolution that contains episodes of pronounced asymmetry. We supplemented our calculations from Section 4.3, which were based on the first 2.5 s in Fig. 4 (DB 1) with two more simulations. These employed databases of the same length but were recorded later. DB 2 covered times [2.5 s; 5.0 s] and DB 3 [5.0 s; 7.5 s]. To provide some measure for the degree of asymmetry, we computed the time-average of the velocity downward components at the probing points close to the bottom. Within DB 1, the mean value of the left-hand side probe was 43% larger than that on the right-hand side. In contrast, it was

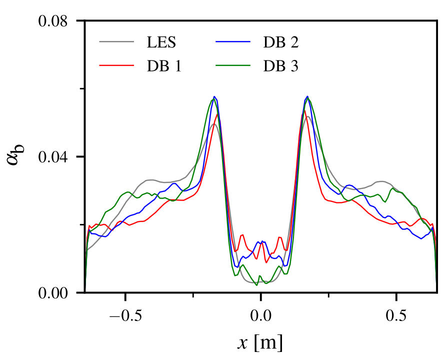

(a)

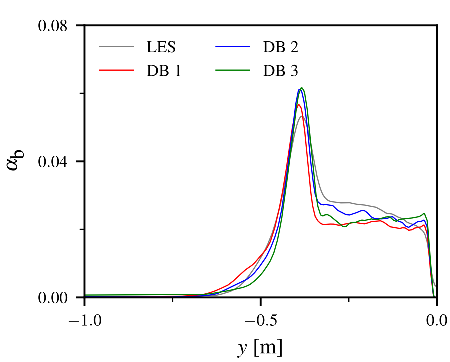

(b)

Fig. 15. Line plots of the time-averaged bubble volume fraction for different choices of recurrence database at high inlet velocity. Both in horizontal (a) and vertical direction (b), rCFD results did not deviate significantly from each other when databases had been obtained from different times in the low-frequency oscillation cycle of the double jet.

93% and 89% lower in DB 2 and DB 3, respectively. However, Fig. 15 demonstrates that no significant differences could be found in the final results of the time-averaged bubble volume fraction. Neither the horizontal line plot at $y = -0.41$ m nor the vertical one at $x = -0.15$ m showed any such indications. While minor deviations were present, there was no obviously best or worst choice between DB 1, 2 and 3 regardless of the fact that especially DB 2 had to balance a much larger degree of asymmetry than DB 1.

At this point, a word of caution is in order. While it seems that augmenting a database with its mirrored counterpart works well to enforce reflection symmetry in cases of slow, asymmetric oscillations, this trick can clearly not be used for processes which are asymmetric by nature or which develop a permanent asymmetry. For example, clogging or misalignment of the SEN may cause such a behavior during continuous casting of steel (Vakhrushev et al., 2022). Given only a short time series, it is not clear how much of an observed lack of symmetry would persist over longer durations. Of course, one might still create a mirrored database and weight it differently, but a reasonable choice of weights could only be determined a posteriori if any relevant long-term data from the process are available.

5. Conclusions, limitations and outlook

In this manuscript, we have reported on fast, data-assisted simulations of bubble transport in a turbulent double-jet at Re = 136 000 and Re = 272 000. Besides the general finding that we could carry out such simulations with speed ups of about 500 and more compared to LES with mostly good accuracy, we think the following insights are particularly worth remembering:

(i) Despite the rapid spatio-temporal variations of the velocity field, we could model bubble transport with time steps and displacements significantly larger than the corresponding scales of the turbulent flow by introducing the bubble displacement field.
(ii) At sufficiently high inlet velocity, the double-jet configuration developed a slow, oscillating mode where one jet pointed more downwards than the other and vice versa. Due to the low frequency of this motion, a short time series was almost necessarily asymmetric and could not describe the full dynamics of the flow. However, augmenting such a database with its mirrored counterpart solved this problem surprisingly well and led to results in close agreement with LES calculations.
(iii) A distance matrix without any pronounced structures characteristic for recurrent states does not imply a random process without memory. The temporal correlations contained in the time series can play a decisive role. Since a fully shuffled recurrence path did not lead to satisfactory results in our case, neither could a stochastic process built only upon the mean flow and its variance.
(iv) Employing two databases corresponding to two different inlet velocities u_{low} and u_{high}, we were able to simulate bubble transport for a time-varying inlet velocity between u_{low} and u_{high} with a recurrence path taking place alternatingly in both databases. Even though the results were only in rough agreement with detailed, costly LES, they gave at least a qualitative impression of the actual flow behavior.

It goes without saying that we had to impose several simplifications in our study, which lend themselves for improvement in future work. In our opinion, the most pressing issue from a methodical point of view concerns the transition between flow regimes as addressed above by (iv). The present interpolation technique works to some degree, but it clearly cannot describe all aspects of the complex dynamics. We will have to answer the questions what it actually means to interpolate *smoothly* between time series, and how the spatial structures of flow fields can be transformed such that they still satisfy the underlying EOMs.

Further possibilities for advancing our work regard the inclusion of additional thermo-physical aspects. While we considered only the bubble phase in this study, we could picture transport processes in the fluid phase in a completely analogous fashion. If heat transfer was simulated over the course of hours, one could determine a realistic temperature distribution and calculate solidification of steel at the domain walls or the SEN (Vakhrushev et al., 2021), which in turn would affect the flow dynamics. However, partial clogging of the SEN could cause an asymmetric flow. It will take a systematic investigation to understand if and how the symmetrization procedure used in this work can be refined so that a temporary asymmetry due to low-frequency jet oscillations can be mitigated without eliminating that induced by the changed inflow behavior.

Overall, we think that the methodology at hand constitutes a useful tool for very fast studies on turbulent and other recurrent flows in general and a first step towards feasible long-term simulations of continuous casting of steel in particular. Nevertheless, a substantial amount of work remains to be addressed such that these simulations become increasingly realistic and finally virtual twins of industrial processes.

Declaration of Competing Interest

The authors declare that they have no known competing financial interests or personal relationships that could have appeared to influence the work reported in this paper.

Acknowledgements

We gratefully acknowledge the funding support of K1-MET GmbH, metallurgical competence center. The research program of the K1-MET competence center is supported by COMET (Competence Center for Excellent Technologies), the Austrian program for competence centers. COMET is funded by the Federal Ministry for Transport, Innovation and Technology, the Federal Ministry for Digital and Economic Affairs and the provinces of Upper Austria, Tyrol and Styria. Beside the public funding from COMET, this research project is partially financed by the industrial partners RHI Magnesita GmbH and Primetals Technologies Austria GmbH.

Appendix A. Properties of the recurrence path

It is possible to establish a close relationship between the temporal average, variance etc. of the original and of the extrapolated time series. The following proof has been originally conducted by one of us in his habilitation thesis (Lichtenegger, 2020) and is reproduced here with the same notation.

The building law Eq. (28) for a recurrence path in a database of N time steps may be turned into a matrix equation. We write the current state of the system as an N-element vector $\boldsymbol{t}$. If the n-th step in the recurrence process corresponds to the l-th entry of the database, it takes the form

$$t_i^{(n)} = \delta_{i,l}. \tag{A.1}$$

The transition to the next step $n+1$ corresponds to the matrix operation

$$\boldsymbol{t}^{(n+1)} = \left(\left(1-\widehat{P}_{\text{jump}}\right)\boldsymbol{S} + \widehat{P}_{\text{jump}}\boldsymbol{J}\right)\boldsymbol{t}^{(n)}, \tag{A.2}$$

where $\widehat{P}_{\text{jump}}$ is a random number with value 0 or 1 with probabilities $1-P_{\text{jump}}$ and P_{jump}, respectively. The shift and jump matrices

$$S_{i,j} = \delta_{i,\text{mod}(j+1,N)} \tag{A.3}$$

$$J_{i,j} = \delta_{i,\text{mod}(\text{sim}(j)+1,N)} \tag{A.4}$$

give rise to a transition to the subsequent state and a jump in the recurrence statistics, respectively. In $\boldsymbol{S}$, the only entries different from 0 are located at an off-diagonal with value 1. $\boldsymbol{J}$ contains entries of 1 for those indices where the most similar state to the column index equals the row index minus 1. The modulo operation both in $\boldsymbol{S}$ and $\boldsymbol{J}$ resembles periodic boundary conditions.

To obtain the probability distribution of states, we replace $\widehat{P}_{\text{jump}}$ with P_{jump}, i.e. instead of a random process returning either 0 or 1, we use a scalar with fixed value $0 \leqslant P_{\text{jump}} \leqslant 1$. The long-term distribution of states is closely connected to properties of the one-step transfer matrix

$$\boldsymbol{T} \equiv (1-P_{\text{jump}})\boldsymbol{S} + P_{\text{jump}}\boldsymbol{J}. \tag{A.5}$$

Assuming that the distribution will converge after repeated application of $\boldsymbol{T}$, we look for that matrix $\boldsymbol{T}^{(\infty)}$ that satisfies $\boldsymbol{T}^{(\infty)} = \boldsymbol{T}^{(\infty)}\boldsymbol{T} = \boldsymbol{T}\boldsymbol{T}^{(\infty)}$. The first equality corresponds to

$$T_{i,j}^{(\infty)} = (1-P_{\text{jump}})T_{i,\text{mod}(j+1,N)}^{(\infty)} + P_{\text{jump}}\sum_k T_{i,k}^{(\infty)}J_{k,j}, \tag{A.6}$$

which is solved by any $t_i^{(\infty)} \equiv T_{i,j}^{(\infty)}$ as long as

$$\forall j : \sum_k J_{k,j} = 1. \tag{A.7}$$

Eq. (A.7) is satisfied by a jump matrix of the form Eq. (A.4), but also by the more general case of possible transitions to several similar states.

The second of the above conditions translates into

$$t_i^{(\infty)} = (1-P_{\text{jump}})t_{\text{mod}(i-1,N)}^{(\infty)} + P_{\text{jump}}\sum_k J_{i,k}t_k^{(\infty)}, \tag{A.8}$$

where we have already inserted $t_i^{(\infty)}$. It can be seen easily that $t_i^{(\infty)} = 1/N$ solves Eq. (A.8) if

$$\forall i : \sum_k J_{i,k} = 1, \tag{A.9}$$

which means that no two different states jump to the same target. This corresponds to a uniform distribution of visited states, which implies that any long-term recurrence path leads to the same statistical moments, in particular mean and standard deviation, as the underlying database.

However, if Eq. (A.9) does not hold, the final distribution $t_i^{(\infty)}$ is not uniform. We expand it into a power series

$$t_i^{(\infty)} = t_{i;0}^{(\infty)} + P_{\text{jump}}t_{i;1}^{(\infty)} + P_{\text{jump}}^2 t_{i;2}^{(\infty)} + \ldots \tag{A.10}$$

If the jump probability P_{jump} is not too large, it suffices to retain only the first non-trivial term in Eq. (A.10). Then, Eq. (A.8) becomes

$$t_{i;0}^{(\infty)} = t_{\text{mod}(i-1,N);0}^{(\infty)} \tag{A.11}$$

$$t_{i;1}^{(\infty)} = t_{\text{mod}(i-1,N);1}^{(\infty)} - t_{\text{mod}(i-1,N);0}^{(\infty)} + \sum_k J_{i,k}t_{k;0}^{(\infty)}. \tag{A.12}$$

With the condition that $t_i^{(\infty)}$ sums up to 1, we get

$$t_{i;0}^{(\infty)} = \frac{1}{N} \tag{A.13}$$

$$t_{i;1}^{(\infty)} = t_{\text{mod}(i-1,N);1}^{(\infty)} - \frac{1-n_i}{N}, \tag{A.14}$$

where $n_i \equiv \sum_k J_{i,k}$ represents the number of states that jump to i. Eq. (A.14) shows that those states are encountered less frequently in the recurrence path, which are not targets from others, even more so in case other such states come before them.

Nevertheless, the resulting distribution $t_i^{(\infty)} \approx t_{i;0}^{(\infty)} + P_{\text{jump}} t_{i;1}^{(\infty)}$ will remain almost uniform if the n_i are not too large and a rather small value is picked for P_{jump}. The latter is limited by the database size, whereas the n_i are determined by the properties of the recurrence process. If jumps aim at the most similar state, this could lead to strongly varying n_i. Alternatively, one could use a jump matrix $\boldsymbol{J}$ where every state jumps to a different target with a high but not necessarily the highest degree of similarity. Such a $\boldsymbol{J}$ may be constructed with the Hungarian algorithm (Kuhn, 1955) if necessary.

References

Abbasi, S., Pirker, S., Lichtenegger, T., 2020. Application of recurrence CFD (rCFD) to species transport in turbulent vortex shedding. Comput. Fluids 196, 104348.
Abbasi, S., Puttinger, S., Pirker, S., Lichtenegger, T., 2020. Recurrence analysis and time extrapolation of a confined turbulent jet using modal decomposition. Phys. Fluids 32 (7), 075115.
Anderson, T.B., Jackson, R.O.Y., 1967. A fluid mechanical description of fluidized beds. Ind. Eng. Chem. Fundam. 6 (4), 527–539.
Baltussen, M., Kuipers, J., Deen, N., 2017. A numerical study of cutting bubbles with a wire mesh. Chem. Eng. Sci. 165, 25–32.
Blais, B., Lassaigne, M., Goniva, C., Fradette, L., Bertrand, F., 2016. A semi-implicit immersed boundary method and its application to viscous mixing. Comput. Chem. Eng. 85, 136–146.
Cecconi, F., Cencini, M., Falcioni, M., Vulpiani, A., 2012. Predicting the future from the past: An old problem from a modern perspective. Am. J. Phys. 80 (11), 1001–1008.
Chen, W., Ren, Y., Zhang, L., Scheller, P.R., 2019. Numerical simulation of steel and argon gas two-phase flow in continuous casting using LES + VOF + DPM model. JOM 71 (3), 1158–1168.
Chen, W., Ren, Y., Zhang, L., 2019. Large eddy simulation on the two-phase flow in a water model of continuous casting strand with gas injection. Steel Res. Int. 90 (4), 1800287.
Cho, S.M., Kim, S.H., Thomas, B.G., 2014. Transient fluid flow during steady continuous casting of steel slabs: Part I. Measurements and modeling of two-phase flow. ISIJ Int. 54 (4), 845–854.
Du, Y., Blocken, B., Pirker, S., 2020. A novel approach to simulate pollutant dispersion in the built environment: Transport-based recurrence CFD. Build. Environ. 170, 106604.
Duraisamy, K., Iaccarino, G., Xiao, H., 2019. Turbulence modeling in the age of data. Annu. Rev. Fluid Mech. 51, 357–377.
Eckmann, J.-P., Kamphorst, S.O., Ruelle, D., 1987. Recurrence plots of dynamical systems. Europhys. Lett 4 (9), 973–977.
Ford, B., Loth, E., 1998. Forces on ellipsoidal bubbles in a turbulent shear layer. Phys. Fluids 10 (1), 178–188.
Georgaka, S., Stabile, G., Star, K., Rozza, G., Bluck, M.J., 2020. A hybrid reduced order method for modelling turbulent heat transfer problems. Comput. Fluids 208, 104615.
Germano, M., 1992. Turbulence: the filtering approach. J. Fluid Mech. 238, 325–336.
Germano, M., Piomelli, U., Moin, P., Cabot, W.H., 1991. A dynamic subgrid-scale eddy viscosity model. Phys. Fluids A 3 (7), 1760–1765.
Goniva, C., Kloss, C., Deen, N.G., Kuipers, J.A.M., Pirker, S., 2012. Influence of rolling friction on single spout fluidized bed simulation. Particuology 10, 582–591.
Hijazi, S., Stabile, G., Mola, A., Rozza, G., 2020. Data-driven POD-Galerkin reduced order model for turbulent flows. J. Comput. Phys. 416, 109513.
Huang, X., Thomas, B., 1998. Modeling of transient flow phenomena in continuous casting of steel. Can. Metall. Q. 37 (3–4), 197–212.
Jain, D., Lau, Y.M., Kuipers, J., Deen, N.G., 2013. Discrete bubble modeling for a micro-structured bubble column. Chem. Eng. Sci. 100, 496–505.
Javurek, M., Wincor, R., 2020. Bubbly Mold Flow in Continuous Casting: Comparison of Numerical Flow Simulations with Water Model Measurements. Steel Res. Int. 91 (12), 2000415.
Jin, X., Cheng, P., Chen, W.-L., Li, H., 2018. Prediction model of velocity field around circular cylinder over various Reynolds numbers by fusion convolutional neural networks based on pressure on the cylinder. Phys. Fluids 30 (4), 047105.
Kloss, C., Goniva, C., Hager, A., Amberger, S., Pirker, S., 2012. Models, algorithms and validation for opensource DEM and CFD-DEM, Prog. Comput. Fluid Dyn. 12 (2012) 140–152, ISSN 1468–4349.
Kuhn, H.W., 1955. The Hungarian method for the assignment problem. Nav. Res. Logist. Q. 2 (1–2), 83–97.
Kuo, J., Wallis, G., 1988. Flow of bubbles through nozzles. Int. J. Multiph. Flow 14 (5), 547–564.
Lawson, N., Davidson, M., 2001. Self-sustanined oscillation of a submerged jet in a thin rectangular cavity. J. Fluid Struct. 15 (1), 59–81.
Lichtenegger, T., 2018. Local and global recurrences in dynamic gas-solid flows. Int. J. Multiphase Flow 106, 125–137.
Lichtenegger, T., 2020. Recurrence CFD: Data-assisted, physics-based simulations of multiphase flows, Habilitation thesis, Johannes Kepler University, Linz, Austria, 2020.
Lichtenegger, T., Miethlinger, T., 2020. On the connection between Lagrangian and Eulerian metrics for recurrent particulate flows. Phys. Fluids 32 (11), 113308.
Lichtenegger, T., Kieckhefen, P., Heinrich, S., Pirker, S., 2019. Dynamics and long-time behavior of gas–solid flows on recurrent-transient backgrounds. Chem. Eng. J. 364, 562–577.
Li, X., Li, B., Liu, Z., Wang, D., Qu, T., Hu, S., Wang, C., Gao, R., 2021. Evaluation of slag entrapment in continuous casting mold based on the LES-VOF-DPM coupled model. Metall. Mater. Trans. B 52 (5), 3246–3264.
Liu, Z., Vakhrushev, A., Wu, M., Kharicha, A., Ludwig, A., Li, B., 2019. Scale-adaptive simulation of transient two-phase flow in continuous-casting mold. Metall. Mater. Trans. B 50 (1), 543–554.
Lui, H.F., Wolf, W.R., 2019. Construction of reduced-order models for fluid flows using deep feedforward neural networks. J. Fluid Mech. 872, 963–994.
Miettinen, J., Howe, A., 2000. Estimation of liquidus temperatures for steels using thermodynamic approach. Ironmak. Steelmak. 27 (3), 212–227.
Mosavati, M., Barron, R.M., Balachandar, R., 2020. Characteristics of self-oscillating jets in a confined cavity. Phys. Fluids 32 (11), 115103.
Murata, T., Fukami, K., Fukagata, K., 2020. Nonlinear mode decomposition with convolutional neural networks for fluid dynamics. J. Fluid Mech. 882, A13.
Nicoud, F., Ducros, F., 1999. Subgrid-scale stress modelling based on the square of the velocity gradient tensor. Flow Turbul. Combust. 62 (3), 183–200.
Pawar, S., Rahman, S., Vaddireddy, H., San, O., Rasheed, A., Vedula, P., 2019. A deep learning enabler for nonintrusive reduced order modeling of fluid flows. Phys. Fluids 31 (8), 085101.
Pirker, S., Lichtenegger, T., 2018. Efficient time-extrapolation of single- and multiphase simulations by transport based recurrence CFD (rCFD). Chem. Eng. Sci. 188, 65–83.
Pirker, S., Puttinger, S., Rössler, R., Lichtenegger, T., 2020. Steel alloy homogenization during Rheinsahl-Heraeus vacuum treatment: conventional computational fluid dynamics, recurrence computational fluid dynamics, and plant observations. Steel Res. Int. 91 (12), 2000214.
Pope, S.B., 2000. Modeling and Simulation. Cambridge University Press, Cambridge, UK.
Puttinger, S., Saeedipour, M., 2022. Time-resolved PIV measurements of a deflected submerged jet interacting with liquid-gas and liquid-liquid interfaces. Exp. Comput. Multiph. Flow 4, 175–189.
Rahman, S.M., Pawar, S., San, O., Rasheed, A., Iliescu, T., 2019. Nonintrusive reduced order modeling framework for quasigeostrophic turbulence. Phys. Rev. E 100 (5), 053306.
Righolt, B.W., Kenjereš, S., Kalter, R., Tummers, M.J., Kleijn, C.R., 2015. Dynamics of an oscillating turbulent jet in a confined cavity. Phys. Fluids 27 (9), 095107.
San, O., Maulik, R., 2018. Extreme learning machine for reduced order modeling of turbulent geophysical flows. Phys. Rev. E 97 (4), 042322.
Shukla, A.K., Dewan, A., 2019. OpenFOAM based LES of slot jet impingement heat transfer at low nozzle to plate spacing using four SGS models. Heat Mass Transf. 55 (3), 911–931.
Sołek, K., Korolczuk-Hejnak, M., Ślęzak, W., 2012. Viscosity measurements for modeling of continuous steel casting. Arch. Metall. Mater. 57 (1), 333–338.
Stabile, G., Ballarin, F., Zuccarino, G., Rozza, G., 2019. A reduced order variational multiscale approach for turbulent flows. Adv. Comput. Math. 45 (5), 2349–2368.
Star, S., Stabile, G., Rozza, G., Degroote, J., 2021. A POD-Galerkin reduced order model of a turbulent convective buoyant flow of sodium over a backward-facing step. Appl. Math. Model. 89, 486–503.
Sujatha, K.T., Jain, D., Kamath, S., Kuipers, J., Deen, N.G., 2017. Experimental and numerical investigation of a micro-structured bubble column with chemisorption. Chem. Eng. Sci. 169, 225–234.
Szekely, J., 2012. Fluid flow phenomena in metals processing. Elsevier.
Thomas, B.G., 2018. Review on modeling and simulation of continuous casting. Steel Res. Int. 89 (1), 1700312.
Trang, C., Ahmed, R., Kaosar, M.G., 2019. Effect of density ratio on the dispersion of particles in a submerged liquid jet. Comput. Part. Mech. 6 (4), 581–589.
Vakhrushev, A., Kharicha, A., Wu, M., Ludwig, A., Tang, Y., Hackl, G., Nitzl, G., Watzinger, J., Bohacek, J., 2021. On modelling parasitic solidification due to heat loss at submerged entry nozzle region of continuous casting mold. Metals 11 (9), 1375.
Vakhrushev, A., Kharicha, A., Karimi-Sibaki, E., Wu, M., Ludwig, A., Nitzl, G., Tang, Y., Hackl, G., Watzinger, J., 2022. Modelling Asymmetric Flow in the Thin Slab Casting Mold under Electromagnetic Brake. Steel Res. Int., 2200088
Wen, Q., Kim, H.D., Liu, Y.Z., Kim, K.C., 2014. Dynamic structures of a submerged jet interacting with a free surface. Exp. Therm. Fluid Sci. 57, 396–406.
Wu, Q., Zhang, Z.-G., Wang, Y., 2019. Numerical investigation of submerged jet flow entrainment behavior adjacent to nozzle. In: Int. Conf. Nucl. Eng. Proc. ICONE 2019.27, The Japan Society of Mechanical Engineers, 2128, 2019.

Xiao, D., Heaney, C., Mottet, L., Fang, F., Lin, W., Navon, I., Guo, Y., Matar, O., Robins, A., Pain, C., 2019. A reduced order model for turbulent flows in the urban environment using machine learning. Build. Environ. 148, 323–337.
Yang, M., Xiao, Z., 2020. POD-based surrogate modeling of transitional flows using an adaptive sampling in Gaussian process. Int. J. Heat Fluid Flow 84, 108596.
Zhang, L., Aoki, J., Thomas, B.G., 2006. Inclusion removal by bubble flotation in a continuous casting mold. Metall. Mater. Trans. B 37 (3), 361–379.
Zimmermann, R., Görtz, S., 2012. Improved extrapolation of steady turbulent aerodynamics using a non-linear POD-based reduced order model. Aeronaut. J. 116 (1184), 1079–1100.